Generic miniband structure of graphene on a hexagonal substrate

J. R. Wallbank,[1] A. A. Patel,[1,2] M. Mucha-Kruczyński,[1] A. K. Geim,[3] and V. I. Fal'ko[1,4]
[1]*Department of Physics, Lancaster University, Lancaster, LA1 4YB, United Kingdom*
[2]*Department of Physics, Indian Institute of Technology Kanpur, Kanpur 208016, India*
[3]*Centre for Mesoscience and Nanotechnology, University of Manchester, Manchester M13 9PL, United Kingdom*
[4]*DPMC, University of Geneva, 24 Quai Ernest-Ansermet, CH1211 Genéve 4, Switzerland*
(Received 19 November 2012; revised manuscript received 1 May 2013; published 4 June 2013)

Using a general symmetry-based approach, we provide a classification of generic miniband structures for electrons in graphene placed on substrates with the hexagonal Bravais symmetry. In particular, we identify conditions at which the first moiré miniband is separated from the rest of the spectrum by either one or a group of three isolated mini Dirac points and is not obscured by dispersion surfaces coming from other minibands. In such cases, the Hall coefficient exhibits two distinct alternations of its sign as a function of charge carrier density.

DOI: 10.1103/PhysRevB.87.245408 PACS number(s): 73.22.Pr, 73.21.Cd, 73.43.−f

I. INTRODUCTION

Recently, it has been demonstrated that the electronic quality of graphene-based devices can be dramatically improved by placing graphene on an atomically flat crystal surface, such as hexagonal boron nitride (hBN).[1–7] At the same time, graphene's electronic spectrum also becomes modified, acquiring a complex, energy-dependent form caused by incommensurability between the graphene and substrate crystal lattices.[8–10] In particular, for graphene placed on hBN, the difference between their lattice constants and crystallographic misalignment generate a hexagonal periodic structure known as a moiré pattern.[2,3,8–10] The resulting periodic perturbation, usually referred to as a superlattice, acts on graphene's charge carriers and leads to multiple minibands[11] and the generation of secondary Dirac-like spectra. The resulting new Dirac fermions present yet another case where graphene allows mimicking of QED phenomena under conditions that cannot be achieved in particle physics experiments. In contrast to relativistic particles in free space, the properties of secondary Dirac fermions in graphene can be affected by a periodic sublattice symmetry breaking and modulation of carbon-carbon hopping amplitudes, in addition to a simple potential modulation. The combination of different features in the modulation results in a multiplicity of possible outcomes for the moiré miniband spectrum in graphene, which we systematically investigate in this paper.

II. SUPERLATTICE HAMILTONIAN

To describe the effect of a substrate on electrons in graphene at a distance, d, much larger than the spacing, a, between carbon atoms in graphene's honeycomb lattice, we use the earlier observation[8–10,12–15] that, at $d \gg a$, the lateral variation of the wave functions of the P^z carbon orbitals is smooth on the scale of a. This is manifested in the comparable sizes of the skew and vertical hopping in graphite and permits an elegant continuum-model description[12–15] of the interlayer coupling in twisted bilayers and the resulting band structure. A similar idea applied to graphene on a hBN substrate[8–10] suggests that a substrate perturbation for Dirac electrons in graphene can be described in terms of simple harmonic functions corresponding to the six smallest reciprocal lattice vectors of the moiré superlattice.

Below, we shall use a similar approach to analyze the generic properties of moiré minibands for electrons in graphene subjected to a substrate with a hexagonal Bravais lattice with a slightly different lattice constant of $(1+\delta)\sqrt{3}a$, $|\delta| \ll 1$, compared to that of $\sqrt{3}a$ for graphene, and a small misalignment angle, $\theta \ll 1$. The moiré pattern harmonics are described by vectors

$$\boldsymbol{b}_{m=0,\ldots,5} = \hat{R}_{\frac{2\pi m}{6}}\boldsymbol{b}_0, \quad \boldsymbol{b}_0 = [1-(1+\delta)^{-1}\hat{R}_\theta]\left(0, \frac{4\pi}{3a}\right), \qquad (1)$$

with length $|\boldsymbol{b}_0| \equiv b \approx \frac{4\pi}{3a}\sqrt{\delta^2+\theta^2}$, which can be obtained from each other by the anticlockwise rotation, $\hat{R}_{2\pi m/6}$. For a substrate with a simple hexagonal lattice or a honeycomb lattice with two identical atoms, the perturbation created for graphene electrons is inversion-symmetric. For a honeycomb substrate where one of the atoms would affect graphene electrons stronger than the other (e.g., such as hBN, for which the occupancy and size of the P^z orbitals are different) the moiré potential can be modeled as a combination of a dominant inversion-symmetric part with the addition of a small inversion-asymmetric perturbation,

$$\begin{aligned}\hat{H} = {} & v\,\boldsymbol{p}\cdot\boldsymbol{\sigma} + u_0 v b f_1(\boldsymbol{r}) + u_3 v b f_2(\boldsymbol{r})\sigma_3\tau_3 + u_1 v\,[\boldsymbol{l}_z \times \nabla f_2(\boldsymbol{r})]\cdot\boldsymbol{\sigma}\tau_3 + u_2 v \nabla f_2(\boldsymbol{r})\cdot\boldsymbol{\sigma}\tau_3 \\ & + \tilde{u}_0 v b f_2(\boldsymbol{r}) + \tilde{u}_3 v b f_1(\boldsymbol{r})\sigma_3\tau_3 + \tilde{u}_1 v[\boldsymbol{l}_z \times \nabla f_1(\boldsymbol{r})]\cdot\boldsymbol{\sigma}\tau_3 + \tilde{u}_2 v \nabla f_1(\boldsymbol{r})\cdot\boldsymbol{\sigma}\tau_3. \qquad (2)\end{aligned}$$

The Hamiltonian $\hat{H}$ acts on four-component wave functions, $(\Psi_{AK}, \Psi_{BK}, \Psi_{BK'}, -\Psi_{AK'})^T$, describing the electron amplitudes on graphene sublattices A and B and in two principal valleys, K and K'. It is written in terms of direct

TABLE I. The inversion-symmetric parameters vbu_i for various models of the moiré superlattice. In the 2D charge modulation model,[9] V_0 is a phenomenological parameter. The G-hBN hopping model in Ref. 10 used the hopping parameter from twisted bilayer graphene. Estimates in Appendix B show that the sets of parameters using a model of point charges attributed to nitrogen sites and for the G-hBN hopping model are very similar.

Model	vbu_0 [meV]	vbu_1 [meV]	vbu_2 [meV]	vbu_3 [meV]
Potential modulation[8]	60	0	0	0
2D charge modulation[9]	$-\frac{V_0}{2}$	0	0	$\frac{\sqrt{3}V_0}{2}$
One-site version of G-hBN hopping[10] (Appendix B 2)	1.6	$\frac{-3.2\delta}{\sqrt{\delta^2+\theta^2}}$	$\frac{3.2\theta}{\sqrt{\delta^2+\theta^2}}$	−2.8
Point charge lattice (Appendix B 1), $0.6 \leqslant \tilde{v} \leqslant 3.4$	$\frac{\tilde{v}}{2}$	$\frac{-\tilde{v}\delta}{\sqrt{\delta^2+\theta^2}}$	$\frac{\tilde{v}\theta}{\sqrt{\delta^2+\theta^2}}$	$-\frac{\sqrt{3}\tilde{v}}{2}$

products $\sigma_i\tau_j$, of Pauli matrices σ_i and τ_j separately acting on sublattice and valley indices. The first term in $\hat{H}$ is the Dirac part, with $\boldsymbol{p}=-i\nabla-e\boldsymbol{A}$ describing the momentum relative to the center of the corresponding valley, with $\nabla\times\boldsymbol{A}=B$. The rest of the first line in Eq. (2) describes the inversion-symmetric part of the moiré perturbation, whereas the second line takes into account its inversion-asymmetric part. In the first line, the first term, with $f_1(\boldsymbol{r})=\sum_{m=0,\ldots,5} e^{i\boldsymbol{b}_m\cdot\boldsymbol{r}}$, describes a simple potential modulation. The second term, with $f_2(\boldsymbol{r})=i\sum_{m=0,\ldots,5}(-1)^m e^{i\boldsymbol{b}_m\cdot\boldsymbol{r}}$, accounts for the A–B sublattice asymmetry, locally imposed by the substrate. The third term, with unit vector $\boldsymbol{l}_z$, describes the influence of the substrate on the A–B hopping: consequently,[16–18] this term can be associated with a pseudomagnetic field, $e\beta=\pm u_1 b^2 f_2(\boldsymbol{r})$, which has opposite signs in valleys K and K'. Each of the coefficients $|u_i|\ll 1$ in Eq. (2) is a dimensionless phenomenological parameter with the energy scale set by $vb\approx 2\pi\sqrt{\delta^2+\theta^2}\gamma_0$, where $\gamma_0\approx 3$ eV is the nearest-neighbor hopping integral in the Slonczewski-Weiss tight-binding model.[19] Concerning the inversion-asymmetric part, the second line in Eq. (2), we assume that $|\tilde{u}_i|\ll|u_i|$. Note that the last term in each line can be gauged away using $\boldsymbol{\psi}\to e^{-i\tau_3(u_2 f_2+\tilde{u}_2 f_1)}\boldsymbol{\psi}$.

Hamiltonian $\hat{H}$ may be used to parametrize any microscopic model compatible with the symmetries of the system (see Appendix A) and the dominance of the simplest moiré harmonics $e^{i\boldsymbol{b}_m\cdot\boldsymbol{r}}$ in the superlattice perturbation. The values that parameters u_i take are listed in Table I for several models of graphene on an hBN substrate, both taken from the recent literature[8–10] and analyzed in Appendix B, including a simple model in which the hBN substrate is treated as a lattice of positively charged nitrogen nuclei with a compensating homogeneous background of electron P^z orbitals. The examples of model-dependent values of parameters u_i, listed in Table I, indicate that the combination of several factors can strongly shift the resulting moiré perturbation across the parameter space in Fig. 1. That is why, in this work, we analyze the generic features of the miniband spectra generated by the moiré superlattice, rather than attempt to make a brave prediction about its exact form for a particular substrate.

In the absence of a magnetic field, the Hamiltonian (2) obeys time-reversal symmetry, which follows from both σ_i and τ_i changing sign upon the transformation $t\to -t$.[20] As a result, $\epsilon_{\boldsymbol{K}+\boldsymbol{p}}=\epsilon_{\boldsymbol{K}'-\boldsymbol{p}}$ and we limit the discussion of minibands to the K valley. Subject to this limitation, the band structure for the inversion-symmetric superlattice perturbation obeys the c_{3v} symmetry. Moreover, using the commutation properties of σ_i, one can establish that

$$\epsilon^{u_0,u_1,u_3}_{\boldsymbol{K}+\boldsymbol{p}}=-\epsilon^{-u_0,-u_1,u_3}_{\boldsymbol{K}-\boldsymbol{p}}=-\epsilon^{-u_0,u_1,-u_3}_{\boldsymbol{K}+\boldsymbol{p}}=\epsilon^{u_0,-u_1,-u_3}_{\boldsymbol{K}-\boldsymbol{p}}. \tag{3}$$

III. GENERIC MINIBAND SPECTRA

To calculate the miniband spectrum for $\hat{H}$ in Eq. (2), we perform zone folding (in the graphene K valley) bringing states with momenta related by the reciprocal lattice vectors $n_1\boldsymbol{b}_1+n_2\boldsymbol{b}_2$ of the moiré pattern to the same point of the superlattice Brillouin zone (sBZ) in Fig. 1(a). Then, we calculate the matrix elements of $\hat{H}$ between those states and diagonalize

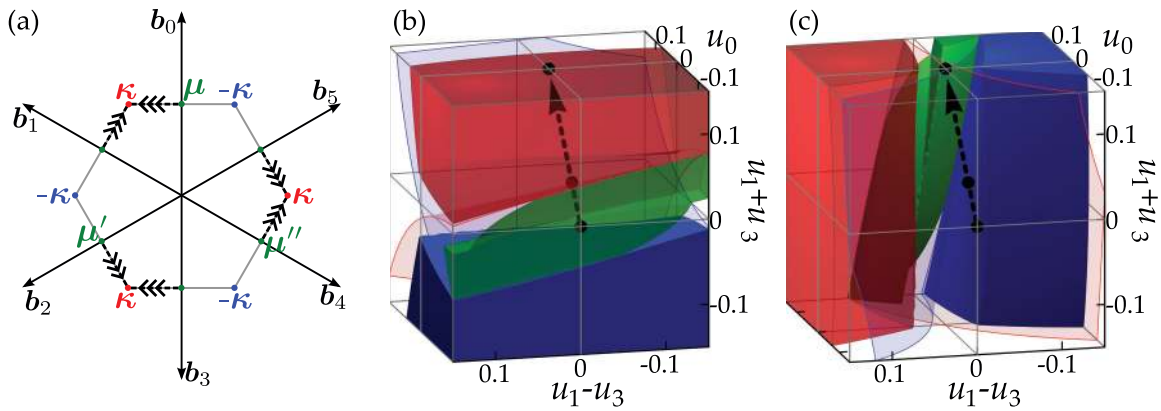

FIG. 1. (Color online) (a) The hexagonal Brillouin zone for the moiré superlattice. (b) Three volumes in the space of the moiré superlattice parameters where the edge of the first miniband, in graphene's valence band, contains an isolated mDP at the $\boldsymbol{\kappa}$ (red) or the $-\boldsymbol{\kappa}$ (blue) points, or three isolated mDPs at the sBZ edge (green). Parameters for which the $\pm\boldsymbol{\kappa}$ point is triple degenerate are shown by the red and blue surfaces. The black dots represent sets of perturbation parameters for which miniband spectra are shown in Fig. 2. (c) The same for the conduction band in graphene.

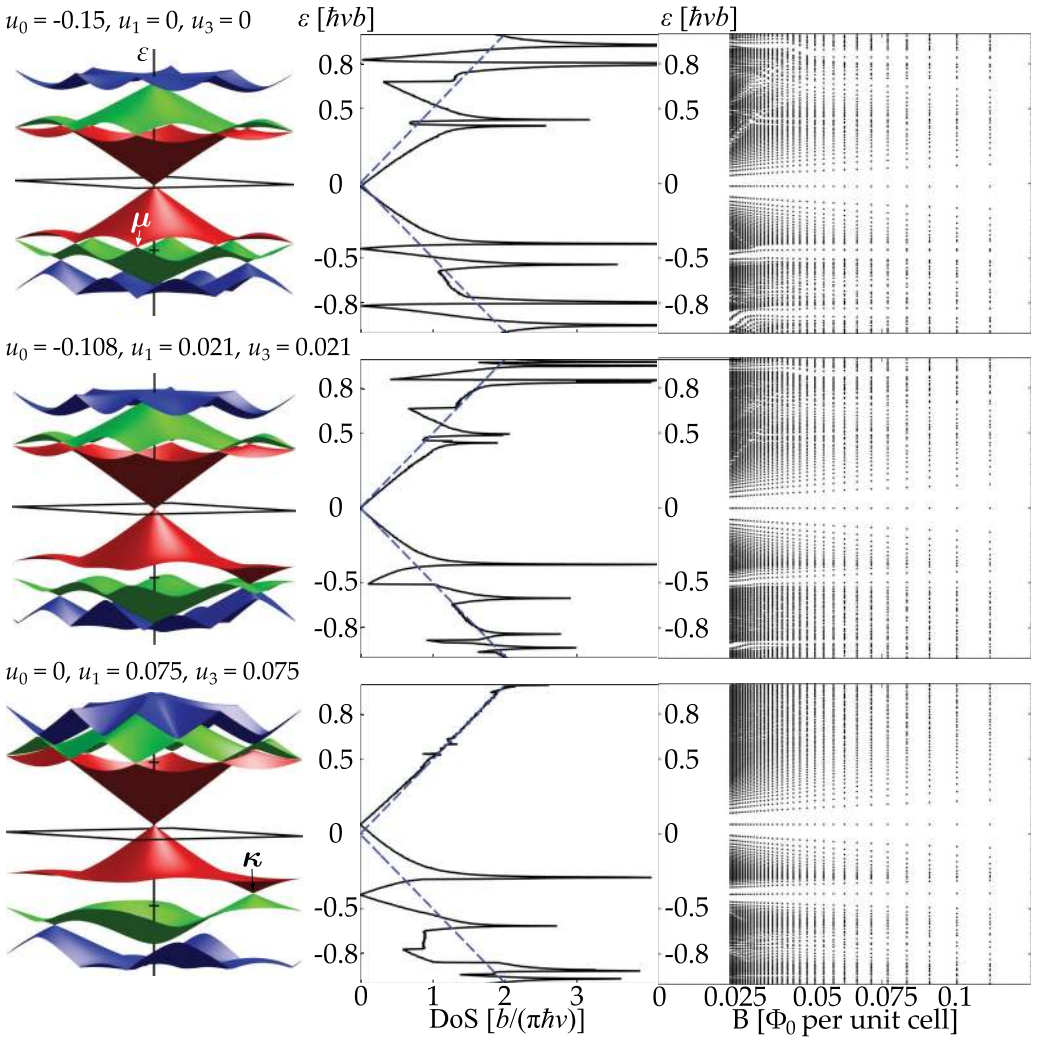

FIG. 2. (Color online) Numerically calculated moiré miniband (left), the corresponding density of states (centre), and Landau level spectrum (right) for electrons in the vicinity of graphene's K point. Here, we use the rhombic sBZ, so that the c_{3v} symmetry of the moiré superlattice spectrum is not obviously seen in the images.

the corresponding Heisenberg matrix numerically exploring the parametric space (u_0,u_1,u_3) of the dominant inversion-symmetric part of the moiré perturbation shown in Figs. 1(b) and 1(c). The size of the matrix is chosen to guarantee the convergence of the calculated energies for the three lowest minibands in both the conduction ($s = +1$) and the valence ($s = -1$) bands. Below, we discuss the generic features of the moiré miniband spectra for the characteristic points in the parametric space (u_0,u_1,u_3), marked using black dots in Figs. 1(b) and 1(c), using both the numerically calculated dispersion surfaces in Fig. 2 and analytical perturbation theory analysis.

For the zero-energy Dirac point in graphene, there are only the original $\boldsymbol{p} = 0$ states in each valley that appear at $\epsilon = 0$ upon zone folding. For all three characteristic spectra shown in Fig. 2, for the inversion-symmetric moiré perturbation, the gapless Dirac spectrum persists at low energies near the conduction-valence band edge with almost unchanged Dirac velocity, $[1 + O(u^2)]v$. The inversion-asymmetric terms $\tilde{u}_i$ are able[10] to open a minigap at the Dirac point.

For the point $\boldsymbol{\mu} = \boldsymbol{b}_0/2$ on the edge of the first sBZ, zone folding brings together two degenerate plane-wave states, $|\boldsymbol{\mu} + \boldsymbol{q}\rangle$ and $|\boldsymbol{\mu} + \boldsymbol{b}_3 + \boldsymbol{q}\rangle$. The splitting of these degenerate states by the moiré potential in Eq. (2) can be studied using degenerate perturbation theory. The corresponding 2×2 matrix, expanded in small deviation $\boldsymbol{q}$ of the electron momentum from each of the three sBZ $\boldsymbol{\mu}$ points[21] has the form

$$\hat{H}_{\boldsymbol{\mu}+\boldsymbol{q}} = vb\begin{pmatrix} E_{\boldsymbol{\mu}} + s\frac{q_y}{b} & H_{12} \\ H_{12}^* & E_{\boldsymbol{\mu}} - s\frac{q_y}{b} \end{pmatrix}, \quad E_{\boldsymbol{\mu}} \approx \frac{s}{2} + \frac{sq_x^2}{b^2},$$

$$H_{12} \approx (su_1 - u_3) - i(s\tilde{u}_1 - \tilde{u}_3) + 2\frac{q_x}{b}(u_0 + i\tilde{u}_0). \qquad (4)$$

For the inversion-symmetric perturbation, the dispersion relation resulting from Eq. (4) contains an anisotropic mini Dirac point (mDP)[8,22,23] with Dirac velocity component $\approx 2u_0 v$ in the direction of the sBZ edge and $\approx v$ in the perpendicular direction. This feature is clearly seen at the $\boldsymbol{\mu}$ point of the first moiré miniband in the valence band, in the top row of Fig. 2. Note that the electron spectrum is not symmetric between the valence and conduction bands and that the mDPs at the $\boldsymbol{\mu}$ point in the conduction band are obscured by an overlapping spectral branch.

Moving in parameter space, e.g., along the line shown in Fig. 1(b), the positions of the three anisotropic mDPs shift along the sBZ edge towards the sBZ corners: either $\boldsymbol{\kappa} = (\boldsymbol{b}_4 + \boldsymbol{b}_5)/3$, or $-\boldsymbol{\kappa}$, as shown by arrowed lines in Fig. 1(a). In general, a spectrum with three isolated mDPs at the sBZ edge is typical for the green volume in the parameter space in Fig. 1(b) for the valence band, or Fig. 1(c) for the conduction band. In contrast, for (u_0,u_1,u_3) in the clear part of the parameter space, mDPs on the edge of the first sBZ are overshadowed by an overlapping spectral branch, as is the case on the conduction band side for all three cases shown in Fig. 2.

For the points in Figs. 1(b) and 1(c) on the red and blue surfaces, the three mDPs reach the $\boldsymbol{\kappa}$ point, forming a triple degenerate band crossing, as in the valence-band spectrum shown in the middle row of Fig. 2, which can be traced using the perturbation theory analysis of the band crossing at $\boldsymbol{\kappa}$ discussed below.

The third line in Fig. 2 shows the third type of spectrum of moiré minibands, characteristic for the red and blue volumes of the parameter space in Fig. 1. The characteristic feature of such spectra consists in a single isolated mDP, at the $\pm\boldsymbol{\kappa}$ point, in the valence band [see Fig. 1(b)] or the conduction band [see Fig. 1(c)].

For the $\boldsymbol{\kappa}$ and $-\boldsymbol{\kappa}$ points, zone folding brings together three degenerate plane-wave states, $|\zeta(\boldsymbol{\kappa}+\boldsymbol{q})\rangle$, $|\zeta(\boldsymbol{\kappa}+\boldsymbol{b}_1+\boldsymbol{q})\rangle$, and $|\zeta(\boldsymbol{\kappa}+\boldsymbol{b}_2+\boldsymbol{q})\rangle$ (where $\zeta = \pm$), whose splitting is determined by

$$\hat{H}_{\zeta(\boldsymbol{\kappa}+\boldsymbol{q})} = vb\begin{pmatrix} \frac{s}{\sqrt{3}}+\frac{sq_x}{b} & w_\zeta & w_\zeta^* \\ w_\zeta^* & \frac{s}{\sqrt{3}}-s\frac{q_x-\sqrt{3}q_y}{2b} & -w_\zeta \\ w_\zeta & -w_\zeta^* & \frac{s}{\sqrt{3}}-s\frac{q_x+\sqrt{3}q_y}{2b} \end{pmatrix},$$

$$w_\zeta \approx \tfrac{1}{2}[(u_0 - 2s\zeta u_1 + \sqrt{3}\zeta u_3) + i\zeta(\tilde{u}_0 + 2s\zeta\tilde{u}_1 - \sqrt{3}\zeta\tilde{u}_3)].$$

For $w_\zeta \neq 0$, the inversion-symmetric terms in $\hat{H}_{\zeta(\boldsymbol{\kappa}+\boldsymbol{q})}$ partially lift the $\zeta\boldsymbol{\kappa}$-point degeneracy into a singlet with energy $(\frac{s}{\sqrt{3}} - 2w_\zeta)vb$ and a doublet with energies $(\frac{s}{\sqrt{3}} + w_\zeta)vb$, so that a distinctive mDP[23] characterized by Dirac velocity $v_{\boldsymbol{\kappa}} = [1 + O(u)]\frac{v}{2}$ (Ref. 9) is always present at $\pm\boldsymbol{\kappa}$ somewhere in the spectrum.[24] This behavior reflects the generic properties of the symmetry group of wave vector $\boldsymbol{\kappa}$, which has the two-dimensional irreducible representation E (corresponding to the mDP) and one-dimensional irreducible representations A_1 and A_2. Note that each isolated mDP is surrounded by Van Hove singularities in the density of states corresponding to saddle points in the lowest energy minibands. The weaker inversion-asymmetric terms, $|\tilde{u}_i| \ll |u_i|$, in the second line of Eq. (2), open a minigap in both types of mDP discussed above.

The appearance of mDPs at the edge of the first miniband results in a peculiar spectrum of electronic Landau levels, as shown on the right-hand side of Fig. 2. Each data point in these spectra represents one of the Hofstadter minibands[25] (with an indistinguishably small width) calculated for rational values of magnetic flux, $\frac{p}{q}\Phi_0$ per moiré supercell following a method in Ref. 14. Using these spectra, one can trace a clearly separated "zero-energy" Landau level related to the isolated $\boldsymbol{\kappa}$-point mDP in the valence band in the bottom row of Fig. 2, in addition to the true zero-energy Landau level at the conduction-valence band edge. The three isolated mDPs on the sBZ edge in the valence band (top row of Fig. 2) also result in a "zero-energy" Landau level, though not as clearly separated and split by the magnetic breakdown occurring at $\Phi \approx 0.1\Phi_0$.

IV. CONCLUSIONS

To conclude, the inversion-symmetric moiré perturbation will result in either the first sBZ separated from the rest of the spectrum by one or three mDPs, or for weak perturbations, will result in overlapping first and higher minibands. The experimental consequences of this can be expected in the optical spectroscopy of graphene on a hexagonal substrate: the presence of mDPs and Van Hove singularities in the density of states should lead to a modulation of the FIR and IR absorption spectra of monolayer graphene, which otherwise, has the flat absorption coefficient of 2.3%.

Another experimental consequence of the moiré minibands would consist in a nonmonotonic variation of the Hall coefficient upon doping the graphene flake with electrons or holes. For example, for those miniband spectra in Fig. 2, where there are isolated mDPs in the valence band, the Hall coefficient would pass through a zero value and change sign at two characteristic densities, n_1 and n_2. At the density n_1, which corresponds to the valence band filled with holes up to the Van Hove singularity, the Hall coefficient will change sign from positive to negative. At the higher density, n_2, which corresponds to a completely filled first miniband, it would repeat the behavior at the neutrality point changing sign from negative to positive. Such behavior is expected to take place for the entire regions of the parametric space painted red, blue, or green in Fig. 1. The relation between these two carrier densities for various types and strengths of moiré perturbations is shown in Fig. 3. For the clear part of the parametric space for which we find substantial overlap between many moiré minibands, such alternations in the sign of the Hall coefficient

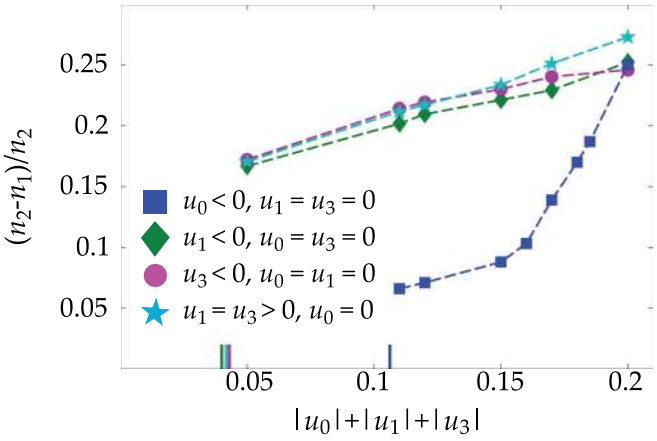

FIG. 3. (Color online) The relation between the two densities at which the Hall coefficient in graphene reverses sign upon its doping with holes. The results are shown for several realizations of moiré superlattice in the parameter range corresponding to either three isolated mDPs on the sBZ edge (squares) or one isolated mDP at the sBZ corner (other symbols). The thresholds for isolation are indicated on the x axis.

would be obscured by the competing contributions from the "electron-like" and "hole-like" branches in the spectrum.

ACKNOWLEDGMENTS

The authors thank F. Guinea, A. MacDonald, E. J. Mele, and P. San-Jose for useful discussions during the 2012 KITP programme *The Physics of Graphene*, where this study was started. We acknowledge financial support from DTC NOWNANO, ERC Advanced Grant *Graphene and Beyond*, EU STREP *ConceptGraphene*, Royal Society Wolfson Research Merit Award, and EPSRC Science and Innovation Award.

APPENDIX A: MOIRÉ SUPERLATTICE SYMMETRY

The point group symmetry of graphene on an incommensurate substrate is given by the intersection of the point group of graphene, c_{6v}, and that of its substrate. For a perfectly aligned ($\theta = 0$) inversion-symmetric substrate, with either a single (dominant) atom per unit cell or two identical atoms arranged in a honeycomb lattice, the point group symmetries of the substrate and graphene coincide. The corresponding Hamiltonian (2), with moiré harmonics orientated as per Fig. 1(a), must necessarily commute with the operators corresponding to the elements of c_{6v}: $\hat{c}_6$, $\hat{s}_x$, and $\hat{s}_y$, which describe $2\pi/6$ rotations and reflections that either exchange or preserve the graphene sublattices. The operators for $\hat{c}_6$ and $\hat{s}_y$ involve the valley exchanging matrices $\tau_{1,2}$ resulting in that the symmetry of the Hamiltonian restricted to the K valley, as well as the K valley band structure, is reduced to $c_{3v} = \{\hat{E}, \hat{c}_3, \hat{s}_x\}$, where $\hat{c}_3 = \hat{c}_6^2$ has no intervalley structure and $\hat{E}$ is the identity. Each of the $\tilde{u}_i$ terms are odd under $\hat{c}_6$, while the u_2 and $\tilde{u}_2$ terms are odd under $\hat{s}_y$, so that these terms are forbidden for the perfectly aligned inversion-symmetric system described above. The point group of substrates with the honeycomb lattice and two nonequivalent atoms per unit cell, such as hBN, only possesses the $\hat{c}_3$ and $\hat{s}_y$ symmetries, which allow inversion-asymmetric parameters $\tilde{u}_{i=0,1,3}$ to take a finite value.

For a finite misalignment angle, the reflection symmetries of graphene and the substrate do not coincide, and the moiré harmonics become misaligned, by an angle ϕ, from those in Fig. 1(a). However, the moiré harmonics may be brought back into alignment using the transformation $\hat{H}(\boldsymbol{r}) \to e^{i\sigma_3\frac{\phi}{2}}\hat{H}(\hat{R}_\phi \boldsymbol{r})e^{-i\sigma_3\frac{\phi}{2}}$, and the u_2 and $\tilde{u}_2$ terms, which are no longer forbidden, may be gauged away. This procedure restores the reflection symmetries to the Hamiltonian, despite their absence in the geometry of the moiré pattern for finite misalignment angle.

The symmetries described above can be used to gain a deeper understanding of the mDPs discussed in the main text. The K valley plane-wave states from the three equivalent sBZ corners, $\zeta\boldsymbol{\kappa}_{n=0,1,2} = \zeta\hat{R}_{2\pi n/3}\boldsymbol{\kappa}$, which form the basis for $\hat{H}_{\zeta\boldsymbol{\kappa}}$, transform into each other on application of symmetry operators of c_{3v}. In the same basis, the symmetry operators acting on $\hat{H}_{\zeta\boldsymbol{\kappa}}$ take the form of matrices

$$\Gamma^{\zeta\boldsymbol{\kappa}}(\hat{c}_3) = \begin{pmatrix} 0 & 0 & -1 \\ -1 & 0 & 0 \\ 0 & 1 & 0 \end{pmatrix}, \quad \Gamma^{\zeta\boldsymbol{\kappa}}(\hat{s}_x) = s\zeta \begin{pmatrix} 1 & 0 & 0 \\ 0 & 0 & 1 \\ 0 & 1 & 0 \end{pmatrix}. \quad \text{(A1)}$$

For the inversion-symmetric superlattice perturbation, the singlet eigenstate of $\hat{H}_{\zeta\boldsymbol{\kappa}}$ is given by $\boldsymbol{v}_s = \frac{1}{\sqrt{3}}(1,-1,-1)$. The action of matrices from Eq. (A1) on this state show that it transforms according to the one-dimensional irreducible representations of c_{3v}: either A_1 for $s\zeta = 1$ or A_2 for $s\zeta = -1$, indicating evenness or oddness under $\hat{s}_x$ respectively. Similarly, the doublet states of $\hat{H}_{\zeta\boldsymbol{\kappa}}$, $\boldsymbol{v}_+ = \frac{1}{\sqrt{3}}(\sqrt{2}, \frac{1}{\sqrt{2}}, \frac{1}{\sqrt{2}})$ and $\boldsymbol{v}_- = \frac{1}{\sqrt{2}}(0,1,-1)$ transform as the two-dimensional irreducible representation E, and their degeneracy is therefore protected by the c_{3v} symmetry.

The three anisotropic mDPs can be understood using the compatibility relations in the group appropriate for the sBZ edge, $c_h = \{\hat{E}, \hat{s}_x\}$. This group only supports one-dimensional irreducible representations A_1 and A_2 with the doublet states reducing as $E = A_1 + A_2$. For a given band, $s = \pm 1$, the split bands at $\boldsymbol{\kappa}$ and $-\boldsymbol{\kappa}$ belong to different irreducible representations of c_h and therefore cannot be joined along the sBZ edge. Instead, if both of these bands are closer to zero energy than the doublet states, they must each be joined to one of the doublet bands at the opposite sBZ corner. Thus, along the sBZ edge, a crossing of the split bands is required, resulting in the mDPs illustrated in the valence band for the top row of Fig. 2.

APPENDIX B: MICROSCOPIC MODELS

1. Point charge lattice model

The point charge model analyzed in this appendix mimics the effect of the quadrupole electric moment of the atoms in the top layer of the substrate. In application to the graphene-hBN system, we neglect the potentials of the quadrupole moments of the boron atom, which have only σ orbitals occupied by electrons, and replace nitrogen sites by a point core charge $+2|e|$ compensated by the spread out cloud of the π electrons, which we replace by a homogeneous background charge density, giving $-2|e|$ per hexagonal unit cell of the substrate. This model gives an example of an inversion-symmetric moiré superlattice. The matrix elements of the resulting perturbation, taken between sublattice Bloch states i and j ($i, j = A$ or B), acting on the low-energy Dirac spinors of the graphene K valley, are given by the long wavelength components of

$$\delta H_{ij} = \frac{-2e^2}{4\pi\epsilon_0}\sum_{\boldsymbol{R}_N}\int dz \frac{L^2\Phi^*_{Ki}(\boldsymbol{r},z)\Phi_{Kj}(\boldsymbol{r},z)}{\sqrt{(\boldsymbol{r}-\boldsymbol{R}_N)^2 + (z-d)^2}} \quad \text{(B1)}$$

$$= \frac{-2e^2}{4\pi\epsilon_0 a}\sum_{\boldsymbol{g},\boldsymbol{g}',\boldsymbol{g}_N} I_{|\boldsymbol{K}+\boldsymbol{g}|,|\boldsymbol{K}+\boldsymbol{g}'|,|\boldsymbol{g}_N|} e^{i(\boldsymbol{g}'-\boldsymbol{g}+\boldsymbol{g}_N)\cdot\boldsymbol{r}} e^{i(\boldsymbol{g}\cdot\boldsymbol{\delta}_i - \boldsymbol{g}'\cdot\boldsymbol{\delta}_j)}.$$

In Eq. (B1), $\boldsymbol{R}_N$ are positions of nitrogen sites and L^2 is the total area of the graphene sheet; $\Phi_{K,i}(\boldsymbol{r},z)$ are Bloch wave

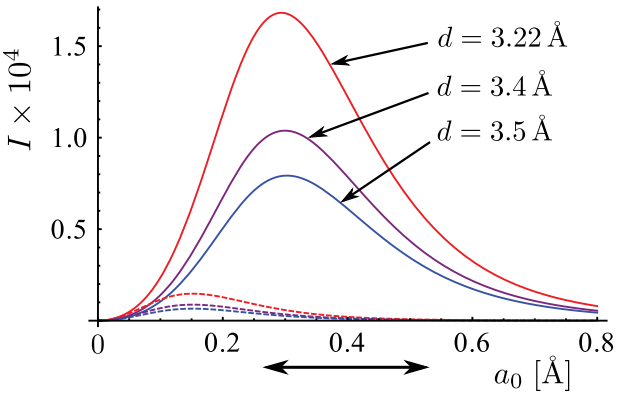

FIG. 4. (Color online) Solid lines show the dimensionless integral I, as a function of the effective Bohr radius of the graphene P^z orbitals, for various choices of interlayer separation d. To demonstrate convergence of the sum in Eq. (B1), dashed lines show I_{2K,K,g_0} for the same values of d.

functions of graphene π electrons exactly at the K point. Then the Fourier transform has been used to write δH_{ij} in terms of a sum over substrate reciprocal lattice vectors, $\boldsymbol{g}_N$, and graphene reciprocal lattice vectors, $\boldsymbol{g}$ and $\boldsymbol{g}'$. Nearest-neighbor vectors, $\boldsymbol{\delta}_{i=A/B}$, are $\boldsymbol{\delta}_A = (0,a)$ and $\boldsymbol{\delta}_B = (0,-a)$, so that $\boldsymbol{K}\cdot\boldsymbol{\delta}_i = 0$. The homogeneous background charge has not been included in Eq. (B1) since its only role is to exclude $\boldsymbol{g}_N = 0$ from the sum. The long wavelength terms in the first exponential of the second line of Eq. (B1) determine $\boldsymbol{b}_m = -(\boldsymbol{g}' - \boldsymbol{g} + \boldsymbol{g}_N)$. The dimensionless integral

$$I_{Q,Q',g_N} = \frac{32a_0^3}{27a^3}\int dq_z dq_z' \frac{\psi^*(Q,q_z)e^{i(q_z-q_z')\cdot d}\psi(Q',q_z')}{g_N^2 + (q_z - q_z')^2}$$

is written in terms of the Fourier transform of the hydrogen-like graphene $P^z(\boldsymbol{r},z)$ orbitals with an effective Bohr radius a_0,

$$\begin{aligned}\psi(Q,q_z) &= \frac{\pi}{a_0^{3/2}}\frac{1}{2\pi}\int d\boldsymbol{r}\, dz\, e^{-i(\boldsymbol{Q}\cdot\boldsymbol{r}+q_z z)}P^z(\boldsymbol{r},z)\\ &= \frac{-64ia_0q_z}{\left[1+4a_0^2\left(Q^2+q_z^2\right)\right]^3}.\end{aligned}$$

The integral I_{Q,Q',g_N} rapidly decays as a function of the magnitude of all its arguments so that we limit the sum in Eq. (B1) to only several terms such that $|\boldsymbol{K}+\boldsymbol{g}| = |\boldsymbol{K}+\boldsymbol{g}'| = |\boldsymbol{K}|$, with $I = I_{K,K,g_0}$, where $g_0 = \frac{4\pi}{3a(1+\delta)}$.

For the graphene layer, $a = 1.42$ Å, and for the graphene-hBN heterostructure, $\delta = 0.018$. The carbon P^z orbitals may have a different effective Bohr radius compared to hydrogen. The range of values quoted for $\tilde{v} = \frac{2e^2}{4\pi\epsilon_0 a}I$ in Table I corresponds to the interval $0.27\text{ Å} \leqslant a_0 \leqslant 0.53\text{ Å}$, indicated by the black double-arrow in Fig. 4. Interlayer separation $3.22\text{ Å} \leqslant d \leqslant 3.5\text{ Å}$ is taken from Ref. 26.

Both the dominance of the simplest moiré harmonics and the finite values for the off-diagonal terms u_1 and u_2 stem from the three-dimensional treatment of the substrate potential. The potential is strongest near the substrate and therefore a greater proportion of the integral I_{Q,Q',g_N} comes from the region near the substrate, where the graphene P^z orbitals are broad and therefore have both rapidly decaying Fourier components and significant overlap with their neighbors. This contrasts with the model employed in Ref. 9, which is based on a two-dimensional substrate potential resulting in $u_1 = u_2 = 0$.

2. Graphene-hBN hopping model

In Ref. 10, Kindermann *et al.* modelled a hBN substrate as a lattice of P^z orbitals onto which the graphene electrons can hop. This treatment, extended from a model of twisted bilayer graphene,[27] assumed equal values for the hopping integral to the boron and nitrogen sites, with the difference between the two sublattices arising from their different on-site energies. Here, we consider an inversion-symmetric version of the hopping model of Ref. 10, assuming that coupling between graphene and the hBN layer is dominated by the hopping to only one of the two sublattices (e.g., boron). Using $\boldsymbol{k}\cdot\boldsymbol{p}$ theory, this coupling can be written as

$$\begin{aligned}\delta\hat{H} &= \hat{H}_{\text{int}}\frac{1}{\epsilon - V - m}\hat{H}_{\text{int}}^\dagger,\\ \hat{H}_{\text{int}} &= \frac{\gamma}{3}\sum_{n=0,1,2} e^{-i\left(\hat{R}_{\frac{2\pi n}{3}}\boldsymbol{\kappa}\right)\cdot\boldsymbol{r}}\begin{pmatrix} e^{i\frac{2\pi n}{3}} \\ e^{-i\frac{2\pi n}{3}}\end{pmatrix}.\end{aligned} \tag{B2}$$

Neglecting a nonoscillatory term, which corresponds to a trivial constant energy shift, Eq. (B2) as applied to graphene electrons in valley K, leads to the moiré Hamiltonian (2), with

$$\{u_{i=0,\ldots,3}\} = \frac{\gamma^2/(vb)}{9(m+V)}\left\{\frac{1}{2}, \frac{-\delta}{\sqrt{\delta^2+\theta^2}}, \frac{\theta}{\sqrt{\delta^2+\theta^2}}, -\frac{\sqrt{3}}{2}\right\}.$$

The parameters of the superlattice perturbation given in Table I of the main text, correspond to $\gamma = 0.3$ eV, $V = 0.8$ eV, and $m = 2.3$ eV, in accordance with Ref. 10. For the perfectly aligned system, we always find $u_2 = 0$, which is a consequence of the reflection symmetries present in the perfectly aligned substrate-graphene system (see Appendix A).

[1] C. R. Dean, A. F. Young, I. Meric, C. Lee, L. Wang, S. Sorgenfrei, K. Watanabe, T. Taniguchi, P. Kim, K. L. Shepard, and J. Hone, Nature Nanotechnology **5**, 722 (2010).

[2] J. Xue, J. Sanchez-Yamagishi, D. Bulmash, P. Jacquod, A. Deshpande, K. Watanabe, T. Taniguchi, P. Jarillo-Herrero, and B. J. LeRoy, Nat. Mater. **10**, 282 (2011).

[3] R. Decker, Y. Wang, V. W. Brar, W. Regan, H.-Z. Tsai, Q. Wu, W. Gannett, A. Zettl, and M. F. Crommie, Nano Lett. **11**, 2291 (2011).

[4] A. S. Mayorov, R. V. Gorbachev, S. V. Morozov, L. Britnell, R. Jalil, L. A. Ponomarenko, P. Blake, K. S. Novoselov, K. Watanabe, T. Taniguchi, and A. K. Geim, Nano Lett. **11**, 2396 (2011).

[5]E. Kim, T. Yu, E. S. Song, and B. Yu, Appl. Phys. Lett. **98**, 262103 (2011).
[6]H. Wang, T. Taychatanapat, A. Hsu, K. Watanabe, T. Taniguchi, P. Jarillo-Herrero, and T. Palacios, IEEE Electron Device Lett. **32**, 1209 (2011).
[7]M. S. Bresnehan, M. J. Hollander, M. Wetherington, M. LaBella, K. A. Thurnbull, R. Cavalero, D. W. Snyder, and J. A. Robinson, ACS Nano **6**, 5234 (2012).
[8]M. Yankowitz, J. Xue, D. Cormode, J. D. Sanchez-Yamagishi, K. Watanabe, T. Taniguchi, P. Jarillo-Herrero, P. Jacquod, and B. J. LeRoy, Nat. Phys. **8**, 382 (2012).
[9]C. Ortix, L. Yang, and J. van den Brink, Phys. Rev. B **86**, 081405 (2012).
[10]M. Kindermann, B. Uchoa, and D. L. Miller, Phys. Rev. B **86**, 115415 (2012).
[11]C.-H. Park, L. Yang, Y.-W. Son, M. L. Cohen, and S. G. Louie, Nat. Phys. **4**, 213 (2008).
[12]J. M. B. Lopes dos Santos, N. M. R. Peres, and A. H. Castro Neto, Phys. Rev. Lett. **99**, 256802 (2007).
[13]R. Bistritzer and A. H. MacDonald, Phys. Rev. B **81**, 245412 (2010).
[14]R. Bistritzer and A. H. MacDonald, Phys. Rev. B **84**, 035440 (2011).
[15]J. M. B. Lopes dos Santos, N. M. R. Peres, and A. H. Castro Neto, Phys. Rev. B **86**, 155449 (2012).
[16]S. V. Iordanskii and A. E. Koshelev, Pis'ma v ZhETF **41**, 471 (1985) [JETP Lett. **41**, 574 (1985)].
[17]M. S. Foster and A. W. W. Ludwig, Phys. Rev. B **73**, 155104 (2006).
[18]A. F. Morpurgo and F. Guinea, Phys. Rev. Lett. **97**, 196804 (2006).
[19]J. C. Slonczewski and P. R. Weiss, Phys. Rev. **109**, 272 (1958).
[20]I. L. Aleiner and K. B. Efetov, Phys. Rev. Lett. **97**, 236801 (2006).
[21]The Hamiltonian in the vicinity of other two inequivalent points on the sBZ edge, $\boldsymbol{\mu}' = \hat{R}_{2\pi/3}\boldsymbol{\mu}$, $\boldsymbol{\mu}'' = \hat{R}_{4\pi/3}\boldsymbol{\mu}$, can be obtained using $H_{\boldsymbol{\mu}+\boldsymbol{q}} = H_{\boldsymbol{\mu}'+\hat{R}_{2\pi/3}\boldsymbol{q}} = H_{\boldsymbol{\mu}''+\hat{R}_{4\pi/3}\boldsymbol{q}}$.
[22]C.-H. Park, L. Yang, Y.-W. Son, M. L. Cohen, and S. G. Louie, Phys. Rev. Lett. **101**, 126804 (2008).
[23]F. Guinea and T. Low, Phil. Trans. R. Soc. A **368**, 5391 (2010).
[24]Note that the spectra derived from $\hat{H}_{\zeta(\boldsymbol{\kappa}+\boldsymbol{q})}$ obey the threefold rotational symmetry.
[25]D. R. Hofstadter, Phys. Rev. B **14**, 2239 (1976).
[26]G. Giovannetti, P. A. Khomyakov, G. Brocks, P. J. Kelly, and J. van den Brink, Phys. Rev. B **76**, 073103 (2007).
[27]M. Kindermann and P. N. First, Phys. Rev. B **83**, 045425 (2011).